University of Bath

Volumetric measurements and simulations of the vortex structures generated by low aspect ratio plunging wings

D. E. Calderon, Z. Wang, I. Gursul, and M. R. Visbal

Articles you may be interested in

Scalable Implicit Flow Solver for Realistic Wing Simulations with Flow Control
Comput. Sci. Eng. **16**, 13 (2014); 10.1109/MCSE.2014.75

A lift formula applied to low-Reynolds-number unsteady flows
Phys. Fluids **25**, 093605 (2013); 10.1063/1.4821520

Aerodynamic effects of wing corrugation at gliding flight at low Reynolds numbers
Phys. Fluids **25**, 071905 (2013); 10.1063/1.4813804

Three-dimensional flow structure and aerodynamic loading on a revolving wing
Phys. Fluids **25**, 034101 (2013); 10.1063/1.4794753

Simulations of dynamics of plunge and pitch of a three-dimensional flexible wing in a low Reynolds number flow
Phys. Fluids **22**, 091901 (2010); 10.1063/1.3481786

Volumetric measurements and simulations of the vortex structures generated by low aspect ratio plunging wings

D. E. Calderon,[1] Z. Wang,[1] I. Gursul,[1] and M. R. Visbal[2]
[1]*Department of Mechanical Engineering, University of Bath, Bath BA2 7AY, United Kingdom*
[2]*U.S. Air Force Research Laboratory, Wright-Patterson Air Force Base, Ohio 45433, USA*

Volumetric three-component velocimetry measurements have been performed on low aspect ratio wings undergoing a small amplitude pure plunging motion. This study focuses on the vortex flows generated by rectangular and elliptical wings set to a fixed geometric angle of attack of $\alpha = 20°$. An investigation into the effect of Strouhal number illustrates the highly three-dimensional nature of the leading edge vortex as well as its inherent ability to improve lift performance. Computational simulations show good agreement with experimental results, both demonstrating the complex interaction between leading, trailing, and tip vortices generated in each cycle. The leading edge vortex, in particular, may deform significantly throughout the cycle, in some cases developing strong spanwise undulations. These are at least both Strouhal number and planform dependent. One or two arch-type vortical structures may develop, depending on the aspect ratio and Strouhal number. At sufficiently high Strouhal numbers, a tip vortex ring may also develop, propelling itself away from the wing in the spanwise direction due to self-induced velocity. © *2013 AIP Publishing LLC*. [http://dx.doi.org/10.1063/1.4808440]

I. INTRODUCTION

A growing desire to miniaturize unmanned air vehicles to a scale close to that of a fly or small bird has encouraged fluid dynamicists to carefully reconsider ways to control flows at these small scales and slow speeds.[1] The proposed operating Reynolds number for a micro air vehicle (MAV) lies in the region of $Re = 10^3$–10^5. Unfortunately, within this regime of Reynolds number, increasing viscous effects promotes the occurrence of separated flows. Conventional fixed wing configurations suffer significantly under these conditions, requiring other means to recuperate aerodynamic performance. One possibility is to imitate the flapping motion that we observe in nature. However, to do so successfully, we need to understand the governing flow physics to then capitalize on the unsteady aerodynamic mechanisms. Essentially, the benefits of flapping a wing, is that it encourages the free shear layer to roll-up and develop into a coherent low pressure structure. Controlling this process can be achieved by controlling the motion of the wing. One may consider the effect of changing the amplitude, frequency, or angle of attack to manage vortex formation. Furthermore, this optimization process may also include the use of various wing profiles, planform shapes, and wing flexibilities. A common goal exists to understand the effects of these variables on the formation and interaction of vortices, allowing us to then use them optimally to exceed the lift performance brought about under steady-state conditions.

Whereas, in nature we regularly observe complex wing kinematics and fluid structure interactions, a more pragmatic solution lies in the imposition of a small amplitude oscillation, in which the wing has one degree of freedom. In our previous work,[2] we studied the effect of small-amplitude plunging oscillations on the aerodynamics of a two-dimensional (2D) airfoil at a non-zero angle of attack. Forced small-amplitude oscillations mimic the aeroelastic vibrations, and the fluid-structure interaction is exploited to enhance lift and delay stall. In this study, we focus on finite aspect ratio (AR) wings that undergo periodic oscillations in the form of a pure plunging motion. However, in our approach, we have small amplitude motion ($h_0/c = O(10^{-1})$) at high frequency (Strouhal number

25, 067102-1

based on the chord length, $St_c = fc/U_\infty = O(1)$), unlike large amplitude motion ($h_0/c = O(1)$) at low frequency ($St_c = fc/U_\infty = O(10^{-1})$) observed in nature. Hence, our kinematics and motivation are different from those of biological flows. Here, we simulate the bending oscillations of a flexible wing by using small-amplitude plunge oscillations of a rigid wing.

Thrust generation by oscillating airfoils was reviewed by Platzer *et al.*[3] Here, in this study, we focus on lift-generating (in a time-averaged sense) flows. Early studies are dominated by two-dimensional airfoils. For example, Freymuth[4] employed a smoke flow visualization technique to characterize the vortex structures over a plunging NACA0015 airfoil. It was set to an angle of attack of $\alpha = 5°$ and oscillated with a normalized amplitude and Strouhal number of $h_0/c = 0.2$ and $St_c = fc/U_\infty = 0.86$, respectively. The downward motion forms a trailing edge vortex (TEV) as well as a weak leading edge vortex (LEV) of opposite rotation. However, the positive geometric angle of attack ensures that at least for this frequency and amplitude, no leading edge vortex is apparently formed during the upward motion of the wing. Freymuth[4] showed that under these conditions, the upper surface LEV travels along the surface of the wing and amalgamates constructively with a trailing edge vortex of similar rotational sense. Lewin and Haj-Hariri[5] explains that the frequency of a plunging airfoil has a significant impact on the fate of the LEV. It may either reinforce or hamper the TEV depending on the time it takes to reach the trailing edge relative to the time it takes to form. This demonstrated to have an impact on at least the thrust capabilities of the wing. Cleaver *et al.*[2] used Particle Image Velocimetry (PIV) to investigate the two-dimensional flow structures of a plunging NACA0012 airfoil, set to an angle of attack of $\alpha = 15°$. Similar deductions were made with respect to the advection of LEVs and the sensitivity to frequency. In addition, specific frequencies with which the wing operated with optimal time-averaged lift were found. At sufficiently high frequency, a lower surface LEV was observed, strong enough to counteract the contributions to lift from the upper surface LEV.

Flows over low aspect ratio wings are fundamentally different to two-dimensional flows. The tip vortex may have a significant impact on the formation and trajectory of the leading edge vortex as well as its efficacy to produce lift.[6] Von Ellenrieder *et al.*[7] performed dye flow visualization on an oscillating rectangular wing with AR = 3.0, illustrating that the result is a complex interaction of vortices. A series of interconnected vortex rings were observed that extended far into the wake of the wing. Similar observations were also made in the simulations.[8] It is interesting to see that at the midspan plane, vortex structures similar to those observed in two-dimensional flows can be found. Dong *et al.*[9] performed a study on the effect of aspect ratio illustrating a correlation between lateral tip vortex spacing and the inclination angles of self-propagating vortex rings.

Yilmaz and Rockwell[10] performed dye flow visualization as well as cross flow PIV measurements on a plunging rectangular flat plate inclined at an angle of $\alpha = 8°$. The wing was studied at an operating Strouhal number of $St_c = 0.34$ and amplitude of $50\%c$. Strong spanwise flows, as well as large streamwise vortices, were reported in the cross-flow measurements. The flows were reproduced in a high fidelity three-dimensional (3D) numerical simulation,[11] to illustrate in great detail the three-dimensionality and evolution of the leading edge vortex. The numerical simulations illustrate that the leading edge vortex has a tendency to anchor itself onto the wing surface, positioning itself vertically, close to the tip of the wing forming an arch-type structure. The cross-flow measurements, forward and aft of this highly three-dimensional structure, result in significantly different cross-flow features, accounting for the reported structures found in the experimental study. As the plunging cycle proceeds, surface pressure contours and iso-surfaces show the progression of the arch vortex towards the symmetry plane of the wing. Eventually the legs of the arch vortex appears to reconnect forming a vortex ring, as it passes the wing, absent of any trailing-edge and tip vortex filaments.

In the present study, in addition to the numerical simulations and planar PIV measurements, we make use of a volumetric three-component velocimetry system to investigate the full three-dimensional flow of a plunging low aspect ratio wing. While simulating such a flow is computationally expensive, it is now possible to simultaneously interrogate an entire region around a wing, using the proposed experimental technique. In view of this, we aim to analyse the effect of Strouhal number on the overall vortex structures that emanate from wings with differing aspect ratio and planform shape.

II. EXPERIMENTAL AND COMPUTATIONAL METHODS

A. Experimental setup

Experiments were carried out in a free-surface closed-loop water tunnel (Eidetics® Model 1520) at the University of Bath, providing a working test section, 1520 mm long, 381 mm wide, and 508 mm deep. Freestream velocities of up to 0.5 ms^{-1} are achievable with a turbulence intensity of less than 0.5%.

The plunging motion is generated by a "shaker mechanism," consisting of an AC 0.37 kW Motovario three-phase motor, using a 5:1 gearbox reduction and a rotary to linear crank mechanism. The crank arm was designed to be long enough to allow the wing to perform a near sinusoidal displacement. The trailing edge location was tracked and subsequently verified to be within 1.25% of the peak to peak amplitude of the sine curve.[12] The angle of attack is fixed throughout the cycle. The frequency is managed by an IMO Jaguar Controller and the amplitude is set by fixing the link bar at various distances from the centre of rotation. An illustration of the rig has been provided in Figure 1.

A total of four wings were tested, comprising of two elliptical and two rectangular flat plates (see Figure 2). While the chord length (c) is kept constant at 100 mm, the half-span (b) is varied to allow further investigation of the effect of aspect ratio. A half-span of 200 mm and 100 mm were explored in this study. The wing profile has a round, semi-circular leading edge and trailing edge, with a thickness-to-chord ratio (t/c) of 0.03. The flow speed was adjusted to give an operating Reynolds number of 2×10^4, based on the root chord length. The oscillatory plunging motion has an amplitude of $h_0 = 0.15c$ and operated within a Strouhal number range of $St_c = fc/U_\infty = 0$–1.35, corresponding to a reduced frequency of $k = \pi fc/U_\infty = 0$–4.24.

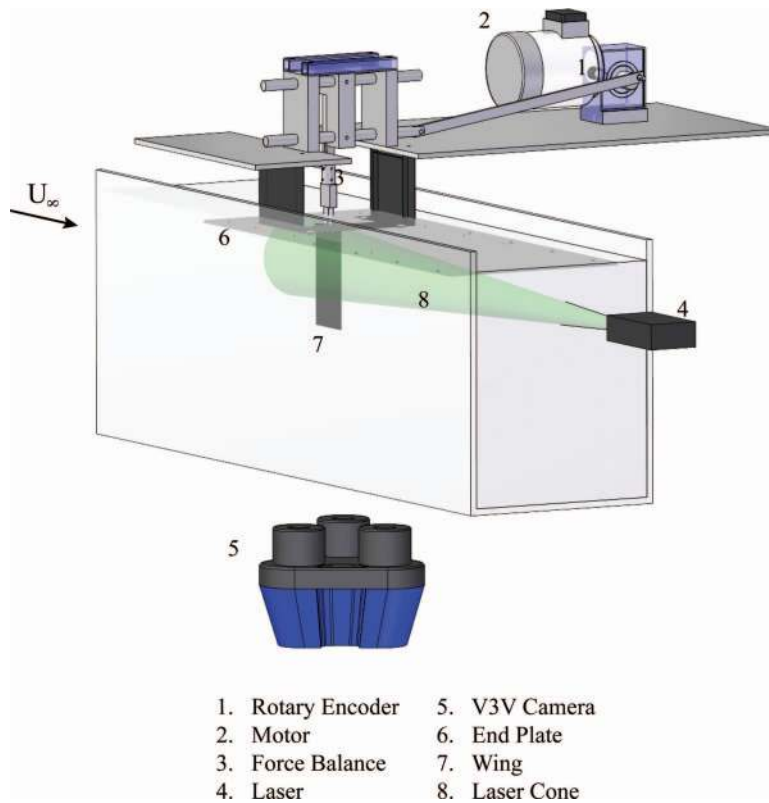|			
1.	Rotary Encoder	5.	V3V Camera
2.	Motor	6.	End Plate
3.	Force Balance	7.	Wing
4.	Laser	8.	Laser Cone

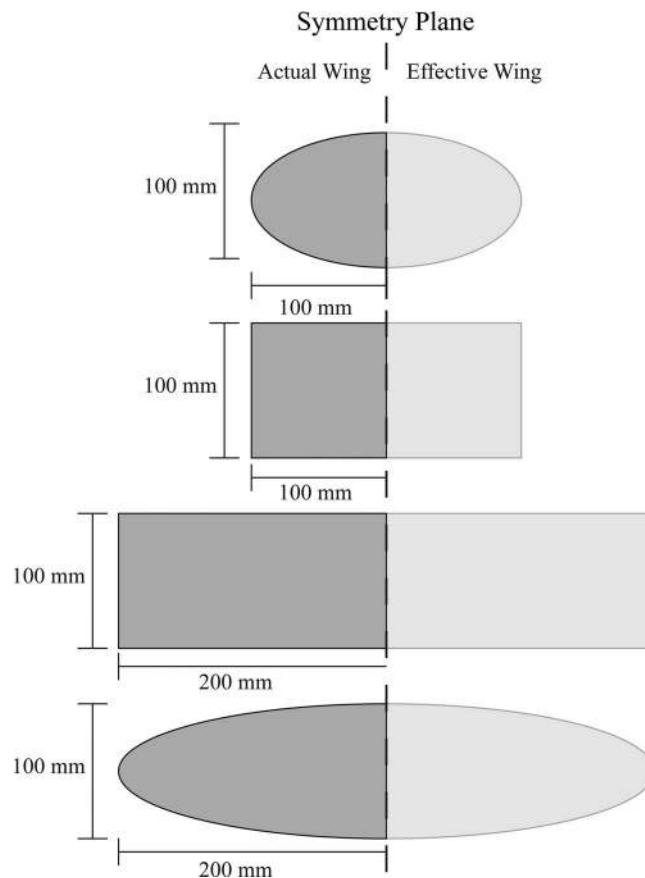FIG. 1. Experimental setup for volumetric velocimetry measurements.

FIG. 2. Schematics of the planform shapes.

B. Force measurements

Force measurements were carried out using a two-component binocular strain-gauge balance. The inherent flexural characteristics of the force balance, necessary for adequate sensitivity to aerodynamic loads, limits the range of frequencies that we were able to study. Two sets of 4 bonded strain gauges were connected to form two Wheatstone bridges with an excitation voltage of ± 6.5 V. Signal conditioning was carried out using an input instrumentation AD624 amplifier, allowing the signal to be zeroed, amplified, and filtered at different stages. The conditioning card provides two gain stages. The input stage has a maximum gain of 500, and the output stage has a finely adjustable gain of 5.54–10.9. A two-pole low pass butterworth filter was set to 30 Hz. Finally, an AD/DA converter prepares the signals for the data acquisition card before being monitored and stored using an in-house program on LabView.

A total of 30 000 data points at a sampling rate of 360 per oscillation cycle, were averaged to generate a mean lift coefficient for a single frequency. This was repeated for various frequencies. It is important to note that within the instantaneous signal there exists an inertia component. The average of this inertia force is zero, allowing us to time-average the instantaneous force to obtain the time-averaged lift force.

C. Volumetric velocity measurements

Flow measurements were acquired using a volumetric three-component velocimetry (TSI V3V) laser system based on the techniques developed by Pereira *et al.*[13, 14] on defocusing digital particle image velocimetry (DDPIV). The volume of interest was illuminated using a dual ND:YAG 200 mJ pulsed laser, equipped with two cylindrical lenses. The two lenses are offset by 90° to allow expansion

in both the horizontal and vertical axes, generating the required laser cone. Seeding is carried out using 50 μm hollow glass particles.

The defocusing concept exploits the ability to use multiple off-axis apertures to generate multiple defocused particle images whose separation distance and location can give an indication of the particles' position in three-dimensional space. Three 4MP 12 bit CCD cameras were placed to form an equilateral triangle whose common focal point defines the most distant plane within the volume of interest. Any particles within the observable domain of these three cameras, set by the intersection of their viewing cones and the reference plane, have a focal point beyond the CCD plane, effectively defocusing the acquired particle image as well as relatively offsetting its location along the common CCD plane with respect to the other CCDs. If the three images were superimposed, a particle in a three-dimensional space would appear thrice, on the vertices of a triangle, corresponding to each of the three cameras. The centre and size of the triangle determine the particle's in-plane and out-of-plane location, respectively.

V3V measurements consist of 4 principal stages: calibration, particle identification, particle tracking, and velocity post-processing. The calibration procedure consists of translating a rectangular plate with 5 mm spaced grid dots across the volume of interest, capturing an image at 5 mm intervals, in order to generate a camera signature graph. This consists of triangles that correspond to the location of the grid center point, in each of the three camera frames, at various distances from the cameras. A 2D particle identification algorithm is performed on each of the 6 captured images, after which a triplet search is performed, whereby a particle is only recognised in 3D space if it can be identified in each camera using the triangles generated during the calibration stage. A pair of laser cones were fired 350–1300 μs apart, depending on freestream velocity and Strouhal number, straddling two neighbouring camera frames. A 3D particle tracking algorithm based on the relaxation method first proposed by Baek and Lee[15] is performed on the triplets identified in each of these camera frames. This essentially uses an iterative process to update the probability of two particles matching between two frames, based on the relative displacements of neighbouring particles. This is outlined in more detail by Pereira *et al.*[16] The velocity post-processing stage uses Gaussian interpolation on the randomly spaced vectors to generate a series of uniformly spaced velocity vectors centred within voxels, 8 mm in size, with 50% overlap. This produced a spatial resolution of around 4%c. The instantaneous velocity has an uncertainty of less than 3%.

Velocity vector fields were processed within MATLAB to compute the desired flow properties, which were then passed over to Tecplot 360 for final analysis. Iso-surfaces were developed predominantly based on vorticity magnitude. However, to distinguish between vortical structures and shear flows, an additional vortex detection algorithm, the Q-criterion, has been put to use. Hunt *et al.*[17] first suggested that a vortex can be characterised based on the second invariant of the deformation tensor. The criterion is based on the ability to decompose the deformation tensor ∇u into symmetrical and antisymmetrical parts, $S = 0.5(\nabla u + \nabla u^{\mathrm{T}})$ and $\Omega = 0.5(\nabla u - \nabla u^{\mathrm{T}})$ (T is the transpose), defining the rate of strain and vorticity tensors, respectively. If $Q = 0.5(\|\Omega\|_E^2 - \|S\|_E^2) > 0$, such that $\| \cdot \|_E$ represents the Euclidean norm, rotational effects dominate and a vortex is said to be identified. Further details on the "Q-criterion" can be found in Jeong and Hussain.[18]

The rotary encoder generates 360 pulses per cycle and allows the user to trigger the LaserPulse synchroniser to fire the laser repeatedly at any of these phase locations. The velocity vectors, presented in this paper, are an average of 140 phase-locked vector fields. The grid interpolation ultimately produced between 25 000 and 35 000 grid vectors within a measurement volume of $164 \times 164 \times 96$ mm. To capture the entire flow field, measurements were obtained by illuminating the upper surface and then the lower surface. This was repeated along the span of the wing, so that the combined measurement volumes contained the near surface flow. In Figure 3, we present the boundaries generated by each of these measurement volumes, for the $b/c = 1$ rectangular wing.

D. Computational approach

For these plunging wing simulations, the governing equations are the full unfiltered compressible Navier-Stokes equations cast in strong conservative form by introducing a general time-dependent curvilinear coordinate transformation $(x, y, z, t) \rightarrow (\xi, \eta, \zeta, \tau)$ from physical to computational space.
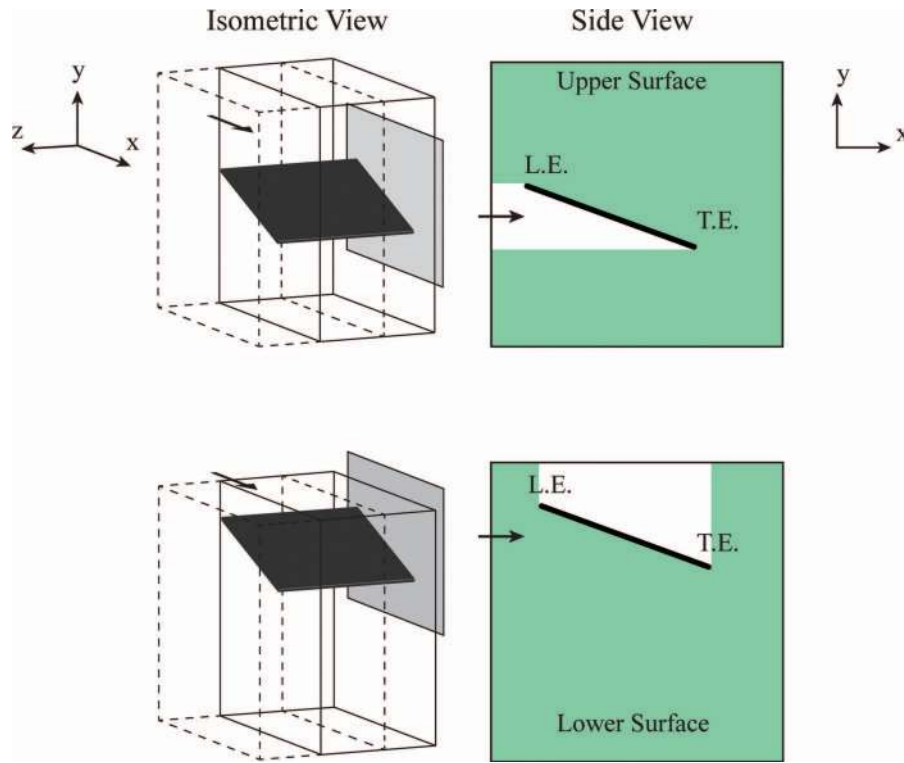
FIG. 3. Isometric and side views of the measurement volumes used to interrogate the entire near surface flowfield of the rectangular $b/c = 1$ wing ($\alpha = 20°$). The green shaded region represents laser illumination.

In terms of non-dimensional variables, these equations can be written in vector notation as

$$\frac{\partial \boldsymbol{Q}}{\partial t} + \frac{\partial \boldsymbol{F_I}}{\partial \xi} + \frac{\partial \boldsymbol{G_I}}{\partial \eta} + \frac{\partial \boldsymbol{H_I}}{\partial \xi} = \frac{1}{\text{Re}} \left[\frac{\partial \boldsymbol{F_v}}{\partial \xi} + \frac{\partial \boldsymbol{G_v}}{\partial \eta} + \frac{\partial \boldsymbol{H_v}}{\partial \xi} \right]. \tag{1}$$

Here, $\boldsymbol{Q} = \frac{1}{J}[\rho\ \rho\boldsymbol{u}\ \rho\boldsymbol{v}\ \rho\boldsymbol{w}\ \rho\boldsymbol{E_t}]^T$ denotes the solution vector and J is the transformation Jacobian. The inviscid and viscous fluxes can be found, for instance, in Anderson.[19] In the expressions above, u, v, w are the Cartesian velocity components, ρ the density, p the pressure, and T the temperature. The perfect gas relationship $p = \rho T/(\gamma M^2)$, Sutherland's law for viscosity, and a constant molecular Prandtl number ($Pr = 0.72$) are also assumed.

The above governing equations correspond to the original *unfiltered* Navier-Stokes equations, and are used without change in laminar, transitional, or fully turbulent regions of the flow. Unlike the standard large eddy simulation (LES) approach, no additional sub-grid stress (SGS) and heat flux terms are appended. Instead, a high-order low-pass filter operator is applied to the conserved dependent variables during the solution of the standard Navier-Stokes equations. This highly discriminating filter selectively damps only the evolving poorly resolved high-frequency content of the solution. This filtering regularization procedure provides an attractive alternative to the use of standard SGS models, and has been found to yield suitable results for several canonical turbulent flows[20,21] on LES-level grids.

All simulations are performed employing the extensively validated high-order FDL3DI Navier-Stokes solver, described in more detail by Visbal and Gaitonde.[22] In this code, a finite-difference approach is used to discretize the governing equations, and all spatial derivatives are obtained employing a 6th-order compact-differencing scheme. In order to eliminate high-frequency spurious components, an 8th-order Pade-type low-pass spatial filtering operator[22] is also incorporated. This filter is applied to the conserved variables along each transformed coordinate direction after each

time step or sub-iteration. For transitional and turbulent flows, this filtering technique provides a high-order implicit LES approach, as previously noted.

For the case of a manoeuvring wing, the grid is moved in a rigid fashion using the prescribed wing motion. To ensure that the Geometric Conservation Law (GCL) is satisfied, the time metric terms are evaluated employing the procedures described in detail in Visbal and Gaitonde.[23]

Computations were carried out employing the low-aspect-ratio plate wing configuration considered in an earlier computational study.[11] The plate has an aspect ratio of two, a uniform thickness $t/c = 0.016$ and all edges are squared-off. This configuration differs from the present experiments, which employ rounded edges. The sensitivity of the plate thickness and edge rounding was studied computationally for a more affordable 2D plunging plate case. No fundamental changes in the overall unsteady flow structure were found for the low Reynolds number and highly forced conditions of interest in this paper.

Computations were performed on a stretched Cartesian mesh containing approximately 30×10^6 grid points. The grid consisted of five zones and had overall dimensions of $440 \times 469 \times 146$ in the streamwise, normal, and spanwise directions respectively. Clustering was provided near the plate in order to capture the complex near-field vortical structure generated by the plunging motion. The mesh was decomposed into a set of 256 overlapped sub-domains or blocks which were assigned to individual processors. A five-point inter-block overlap was employed in order to retain high-order numerical accuracy.

The boundary conditions were prescribed as follows. Along the entire wing surface, a no-slip adiabatic condition was employed in conjunction with a zero normal pressure gradient. The surface velocity components were determined from the imposed plunging motion. In order to improve spatial resolution with available computational resources, the flow was assumed to be symmetric about the wing centerline. This simplification was considered based on examination of previous plunging wing experiments by Yilmaz and Rockwell.[10] Furthermore, the present experiments are performed for a half-wing configuration with a small gap as noted earlier. On the far field boundaries, located approximately 100 chords away from the wing, freestream conditions were specified. It should be noted that prior to reaching this boundary, the grid is stretched rapidly. This stretching in conjunction with the low-pass spatial filter provides a buffer-type treatment found to be quite effective in reducing spurious reflections.

Plunging simulations were started from the previously computed static solution at the corresponding mean angle of attack. Simulations were then advanced in time for ten cycles, and phase-averaged information was obtained from the last eight cycles to isolate start-up transients. A very small computational time step $\Delta t U_\infty / c = 6.158 \times 10^{-5}$ was prescribed in order to provide sufficient temporal resolution of the fine-scale transitional vortical structure. This value of Δt corresponded to 25 000 time steps per cycle for a Strouhal number $St_c = 0.65$. Finally, all computations were performed employing a low freestream Mach number $M = 0.05$, as required with the present compressible Navier-Stokes solver.

III. RESULTS AND DISCUSSION

A. Lift measurements

Time-averaged lift measurements are presented in Figure 4 as a function of Strouhal number (St_c). The respective wings were set to a fixed geometric angle of attack of $\alpha = 20°$ which corresponds, in each case, to that of a post-stall regime for the stationary wing. The static lift curves as a function of angle of attack are given elsewhere.[5] As seen in Figure 4, for all wings the lift coefficient for the stationary case was between 0.76 and 0.80. It is also seen in Figure 4 that both rectangular and elliptical wings with $b/c = 2$ exhibit clear peaks at specific Strouhal numbers. Cleaver *et al.*[2] showed that at particular frequencies, experimentally, a NACA0012 plunging airfoil experiences localised maxima in time-averaged lift. It was postulated that the local maxima occur due to the resonance with the harmonics of the vortex shedding frequency of the stationary wing. Calderon *et al.*[25] demonstrated that the phenomenon continues to exist in the low aspect ratio case for different angles of attack in the post-stall region. Hence, it appears that a similar mechanism is at work for
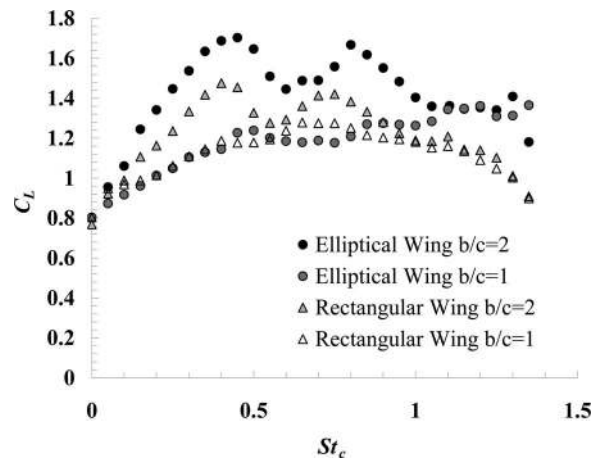
FIG. 4. Time-averaged lift coefficient for various wings at angle of attack $\alpha = 20°$; amplitude $h_0 = 0.15c$.

2D and 3D wings. In fact, even at very low Reynolds numbers ($Re = 300$–500), there is evidence of vortex shedding from low aspect ratio wings[6] and periodic excitation at a frequency slightly less than the natural frequency of vortex shedding can lead to enhanced lift.[26]

It appears that the added three-dimensional effects from the tip vortex, nonetheless, attenuate to some degree the existence of this phenomenon. Peaks have been identified in both rectangular and low-sweep delta wing planforms[24] and in Figure 4 we demonstrate that they too exist in elliptical wings. It is interesting to observe that the frequencies at which these peaks occur are quite similar to the rectangular wing. Furthermore, the $b/c = 2$ elliptical wing appears to have better lift performance, than the $b/c = 2$ rectangular wing. This fails to be the case for the lower aspect ratio wings, for which the time-averaged lift curve appears to be absent of any prominent peak, especially in the case of the elliptical planform. At higher Strouhal numbers, both rectangular wings exhibit a reduction in lift, approaching performance levels similar to that of the stationary case. In the case of the elliptical wings, the degradation in performance is far more gradual.

B. Comparison of experiments and simulations

A comparison of the computed and experimental results for the $b/c = 1$ rectangular wing plunging at $St_c = 0.65$ is shown in Figures 5 and 6. In Figure 5, the flow is reflected about the wing centerline ($z = 0$) with the assumption of lateral symmetry. (Note that the calibration process near the end plate resulted in a loss of 3 mm at the root of the wing. Therefore, a discontinuity in the measured vortical structures appears near the symmetry plane in Figure 5.) The three-dimensional phased-averaged flow structure is represented using an iso-surface of the Q-criterion ($Qc/U_\infty = 20$). It should be noted that the computational grid is much finer than the prescribed spatial resolution in the experimental measurements, and therefore the computational results were filtered onto the PIV mesh using the procedure described elsewhere.[27] Despite the fact that many more cycles have been used in the experiment to achieve a smoother phase-averaged representation, overall good agreement is observed between experiments and computations in terms of the main flow features.

As the wing plunges downward (Figures 5(b)–5(e)), a leading-edge vortex is formed due to the increasing effective angle of attack. This vortex is fairly coherent in the spanwise direction and is pinned at the front corners of the plate. In the experiments, the vortex does not extend all the way to the symmetry plane as explained above. The formation and strengthening of the tip vortices is also observed during the downstroke motion. The tip vortices join with the trailing-edge vortex (containing vorticity generated on the bottom plate surface) to form a vortex loop extending from one wing front corner to the opposing edge. Near the end of the downstroke (Figures 5(f) and 5(g)), spanwise undulations of the leading-edge vortex are observed. As the wing moves upwards (Figures 5(h)–5(k)), the leading-edge vortex detaches from the wing front corners. Following its
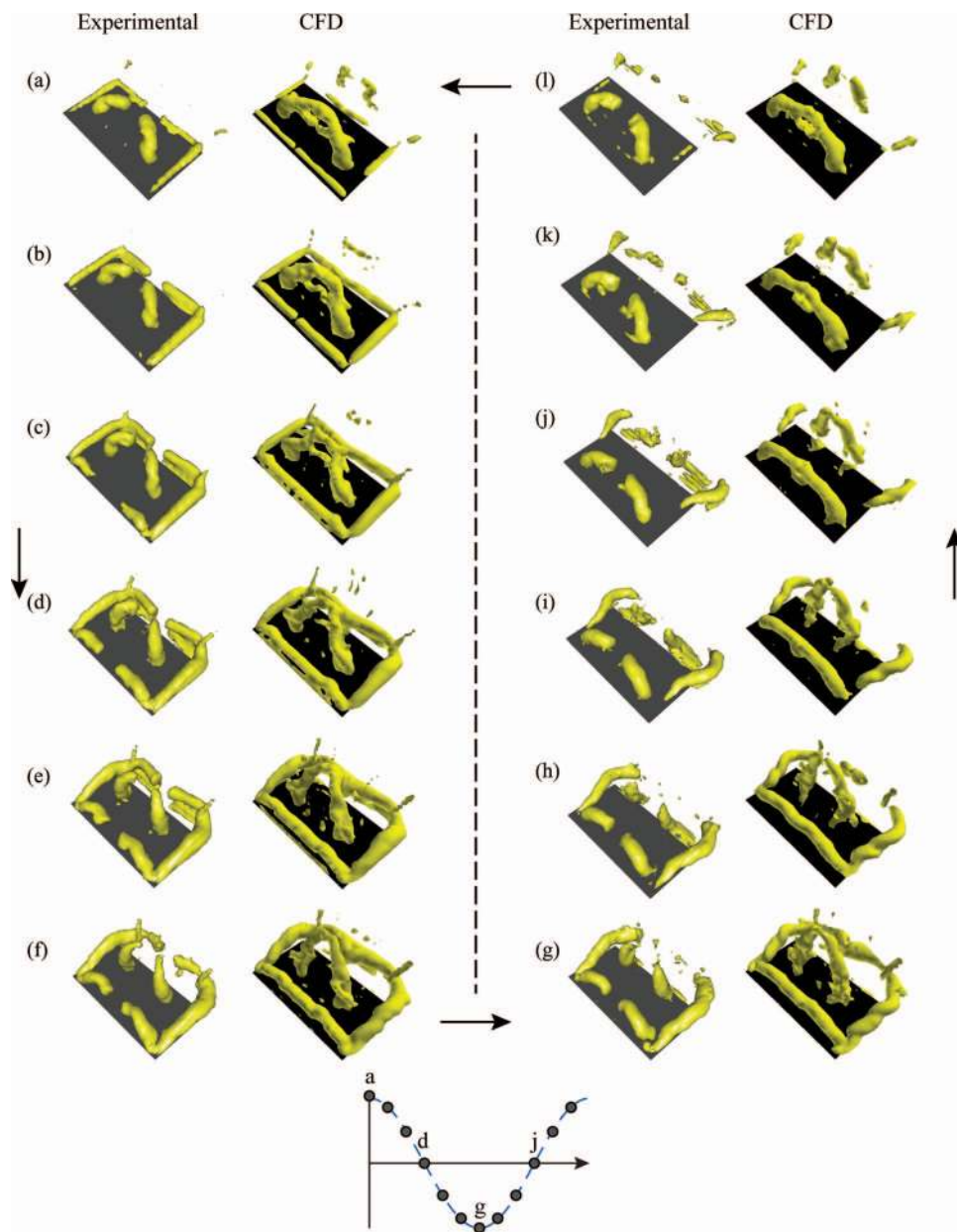
FIG. 5. (a)–(l) A 12-phase comparison between CFD and experimental results, for the $b/c = 1$ rectangular wing at $St_c = 0.65$, showing $Qc/U_\infty = 20$.

detachment, the leading-edge vortex evolves into an "arch-type" structure similar to that found by Visbal.[11] The legs of the arch-vortex move downstream and towards the wing centerline and the vortex height also increases. During the upstroke, the tip vortices appear to breakdown and the trailing-edge vortex is shed into the wake. Although the basic flow structures are similar in the experiments and computations, there appears to be a small relative shift. For instance, in Figure 5(k), the legs of the vortex are closer to the centerline in the experiments. Also in Figure 5(g), the computed arch vortex is slightly upstream of the experimental counterpart. For this relatively moderate-amplitude high-frequency heaving motion, the arch-vortex remains over the wing well into the next plunging cycle. For instance, in Figure 5(d), the arch vortex is still located near the mid-chord and does not reach the plate trailing edge until the initiation of the subsequent upstroke (Figure 5(h)).
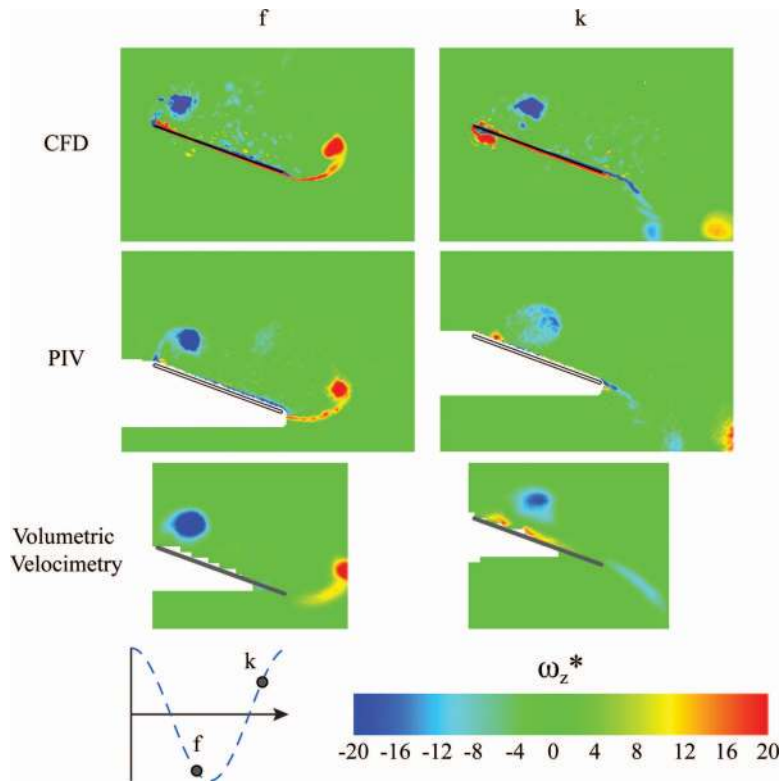
FIG. 6. A comparison of non-dimensional spanwise vorticity, $\omega_z^* = \omega_z c/U_\infty$, between CFD, PIV, and volumetric velocimetry measurements, at a plane halfway along the span of the $b/c = 1$ rectangular wing ($z/c = 0.5$).

In order to make more quantitative comparisons, in Figure 6 we plot spanwise vorticity results together with those obtained with the 2D-PIV system. Phase-averaged measurements were acquired at a specified location along the span of the wing ($z/c = 0.5$). Again, there appears to be a good overall agreement with respect to vortex size, location, and strength. However, finer shear layer structures appear to be poorly resolved with the volumetric system. This can be explained by the difference in the grid spacing.

The case shown so far consists of the formation of a leading edge vortex that appears to "detach," or move away, from the surface of the wing, as it is subject to the oncoming flow. It is important to note that the gradual convection of this vortex towards the wing centreline poses a significant problem for the 2D-PIV user. While 2D-PIV provides a relatively quick and high-resolution procedure, the user is left unknowing whether an apparent reduction in vortex strength is the result of vortex breakdown or reorientation of the vortex filament, both of which would affect the spanwise component of vorticity, ω_z.

C. Effect of Strouhal number

In Figures 7(a)–7(f), we investigate the effect of Strouhal number on the developing vortex structures by showing vorticity iso-surfaces of the plunging $b/c = 1$ rectangular wing, oscillating at a range of Strouhal numbers. In Figure 7, Strouhal number is organized by column and cycle progression (phase) by row. We note that as the time scale diminishes with increasing Strouhal number, the separation distance between leading edge vortices, formed in adjacent cycles, also diminishes. At a Strouhal number of $St_c = 0.4$, which is closer to the value of $St_c = 0.34$ studied by Yilmaz and Rockwell[10] and Visbal,[11] a single plunging cycle is enough to allow the leading edge vortex to pass over the entire wing. This prevents the appearance of multiple vortices and subsequently minimizes any interaction. We also observe that the LEV undergoes rapid growth and
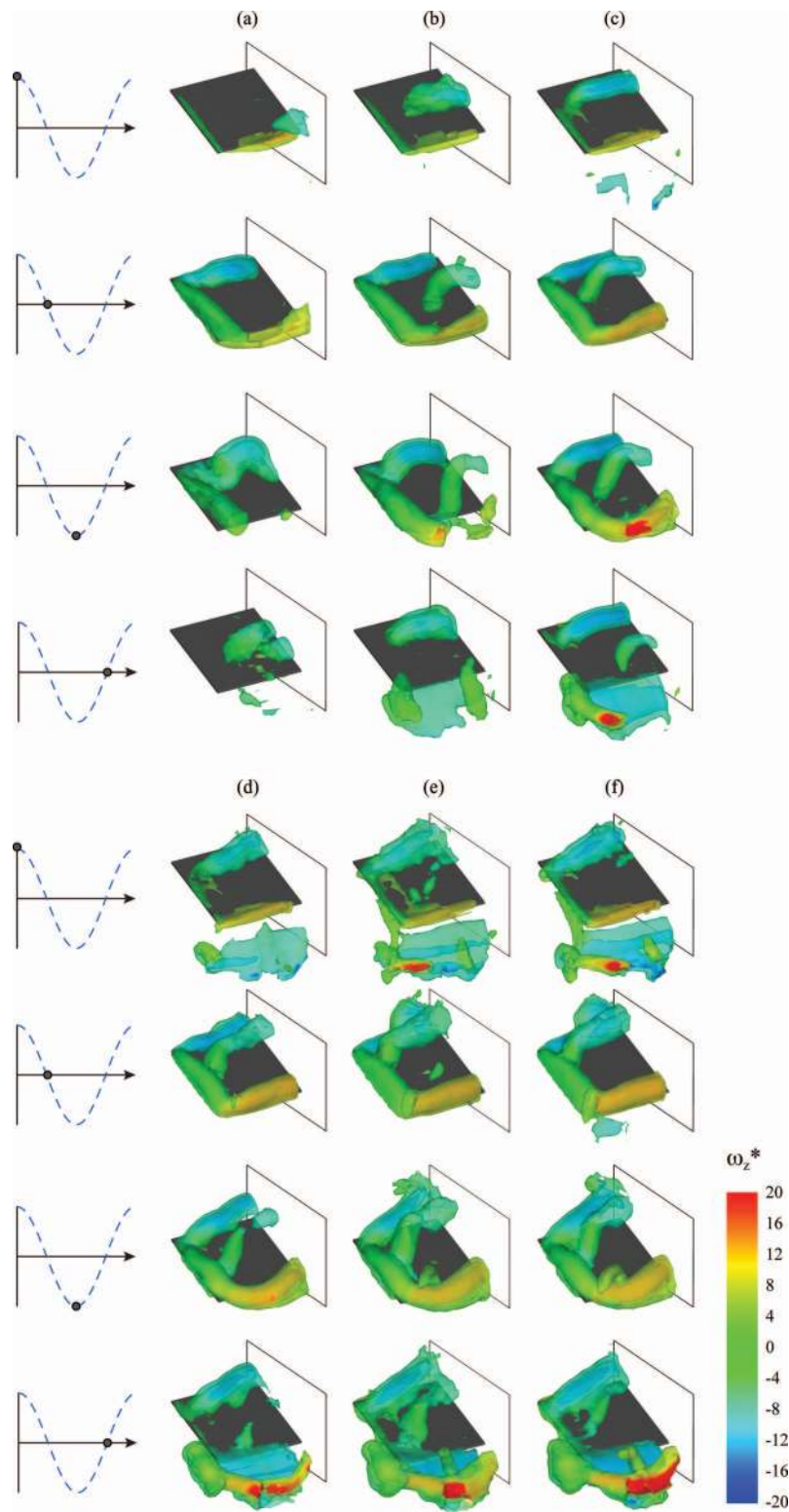
FIG. 7. (a)–(f) Isometric views of the vortices that surround the $b/c = 1$ rectangular wing at 4 phases in the cycle for various frequencies: (a) $St_c = 0.4$, (b) $St_c = 0.6$, (c) $St_c = 0.8$. (d) $St_c = 1.0$, (e) $St_c = 1.2$, and (f) $St_c = 1.35$. Iso-surfaces represent constant vorticity magnitude, $|\omega^*| = |\omega c/U_\infty| = 8$, 15, and 25 and colour maps indicate spanwise vorticity.

deforms significantly at the bottom of the oscillation ($t^* = 0.5$). Increasing the Strouhal number appears to have a significant effect on the compactness of the vortex as well as the deformation of the filament. This is evident when comparing the LEV for $St_c = 0.4$ and 0.8. It is interesting to see that the path of the LEV anchor point seems to be highly Strouhal number dependent, appearing closer to the tip of the wing with increasing Strouhal number. This effect is far more evident at the higher frequencies of $St_c = 1.0$–1.35, shown in Figures 7(d)–7(f). At these frequencies, rather than it developing into an arch-shaped structure, the vortex filament takes a sharp 90° turn from the surface of the wing. As the cycle progresses, the gradual inboard movement of the leading edge vortex becomes less evident. Also, note that the LEV becomes oblique to the leading-edge at $t^* = 0$ for high Strouhal numbers, rather than being parallel to it, as for low Strouhal numbers. It is interesting to observe that this phenomenon of vortex tilting was not observed for the high Strouhal number case investigated by Visbal.[28] Bearing in mind a much smaller amplitude of $h_0 = 0.0625c$ was investigated, it appears this may be limited to high amplitude high frequency motions.

It is also interesting to observe vorticity iso-surfaces from a side view; this is presented in Figures 8(a)–8(f). At the lower Strouhal numbers, the inboard portion of the LEV travels further as the outboard portion near the tip stretches (see Figure 8(b) at the top of the oscillation), which is similar to what was observed by Visbal.[11] At higher Strouhal numbers, this stretching near the tip is notably attenuated (see Figure 8(f) at the top of the oscillation). We also observe the formation of a lower surface leading edge vortex at the top of the oscillation. This is similar to the observations of Visbal.[11] It first appears at $St_c = 0.8$ and grows rapidly as the Strouhal number is increased. For $St_c = 0.8$, the motion induced incidence is around 37°. Time-averaged lift measurements in Figure 4, indicate a reduction in lift beyond $St_c = 0.75$. The formation of a lower surface LEV, which effectively provides a suction force countering the effects of the upper surface LEV, shows good correlation with the characteristics of the mean lift curve.

Considering the low aspect ratio of the wing as well as the high mean angle of attack, it is important to consider the nature and possible role of the tip vortex on the ensuing near surface flow structures. Regardless of Strouhal number, the tip vortex forms in-phase with the oscillation, developing during the downward motion of the wing. While the upstream section of the tip vortex is pinned to the front corners, the downstream section is seamlessly connected to the trailing edge vortex. The first half of the downstroke sees a completely attached tip vortex, whose downstream portion begins to "detach" during the second half of the downstroke (see, for example, Figure 8(c)). Lower plunging frequencies promote the detachment process due to the high geometric angle of attack and early shedding of the trailing edge vortex. It is also interesting to observe that halfway through the upstroke, a vortex ring appears close to the rear corner of the wing (see Figures 8(d)–8(f)).

In Figure 9, we present iso-surfaces of Q-criterion at $t^* = 0.75$ in the cycle to further explore the vortex ring. Altough the iso-surfaces represent a constant Q-criterion value, colour maps have been superimposed to illustrate any variation in the streamwise component of vorticity, ω_x. This allows the reader to differentiate between tip vortices formed during the downstroke and upstroke. It is interesting to consider that increasing the Strouhal number has the effect of increasing the effective angle of attack, which has a direct consequence on the tip vortex. At higher Strouhal numbers, the effective angle of attack is negative enough during the upstroke to promote the formation of a tip vortex of opposite sign, from the lower surface, despite the large geometric angle of attack. The Q-criterion effectively isolates a vortex from its adjacent shear flow, to allow one to more easily visualize the vortex structure. It is now evident that the vortex ring consists of an interaction between lower and upper surface tip vortices. The comparison at various Strouhal numbers suggests that the phenomenon is associated with high frequency oscillations. In Figure 10, a lower surface isometric view of the Q-criterion iso-surface at $t^* = 0.75$ is provided to clarify how the vortex ring is formed. A complex interaction occurs in which the lower surface tip vortex remains connected to the trailing edge vortex and its fine shear layer structures, while a significant portion of it bends around to join with the upper surface tip vortex.

In Figure 11, we consider a cross-stream slice through the tip vortex ring, $0.1c$ from the trailing edge. We observe that with increasing frequency, both the upper and lower surface tip vortex strengthen. Moreover, their close interaction results in an induced velocity with a strong spanwise component. This results in a spanwise expansion of the wake vortex system at least in the vicinity
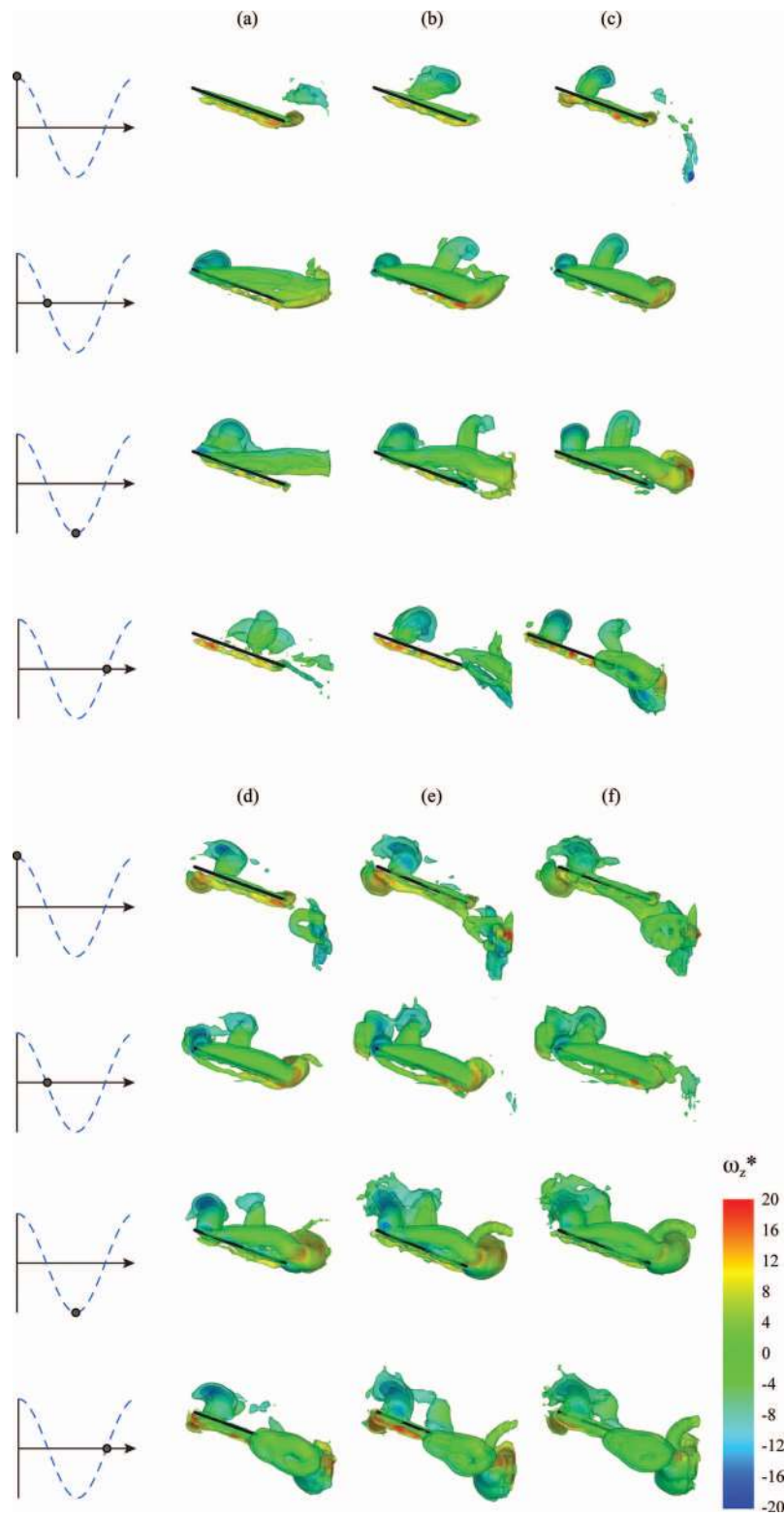
FIG. 8. (a)–(f) Side views of the vortices that surround the $b/c = 1$ rectangular wing at 4 phases in the cycle for various frequencies: (a) $St_c = 0.4$, (b) $St_c = 0.6$, (c) $St_c = 0.8$. (d) $St_c = 1.0$, (e) $St_c = 1.2$, and (f) $St_c = 1.35$. Iso-surfaces represent constant vorticity magnitude, $|\omega^*| = |\omega c/U_\infty| = 8$, 15, and 25 and colour maps indicate spanwise vorticity.
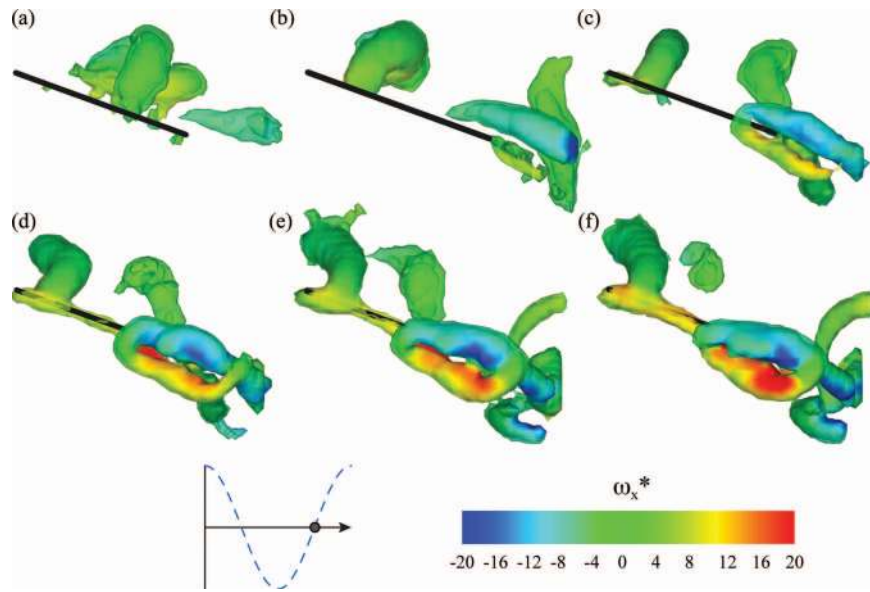
FIG. 9. A side view of the Q-criterion iso-surfaces surrounding the $b/c = 1$ rectangular wing at $t^* = 0.75$ for various frequencies: (a) $St_c = 0.4$, (b) $St_c = 0.6$, (c) $St_c = 0.8$, (d) $St_c = 1.0$, (e) $St_c = 1.2$, and (f) $St_c = 1.35$. Iso-surfaces represent constant Q-criterion, $Qc/U_\infty = 15$, 30, and 45 and colour maps represent streamwise vorticity.

of the wing. It should be noted that in the previous work on pitching wings at high Strouhal number, wake vortices have been observed to undergo spanwise compression,[9, 29] for which tip vortices have an induced velocity directed towards the symmetry plane of the wing. Although, we cannot conclude on the manner in which the wake vortices evolve further downstream, the tip vortices, do, at least in the vicinity of the trailing edge, seem to differ significantly from these studies.

Previous findings of vortex rings report vortex loops consisting of leading-edge vortex, tip vortex, and trailing-edge vortex. Vortex rings have in the past been visualized using a similar volumetric velocimetry technique.[30] The literature also provides flow visualizations[7, 29] and numerical simulations[8, 9] that exemplify the vortex rings that one generally encounters downstream of an oscillating wing. However, the composition of these vortex loops is fundamentally different from the *tip vortex ring* discovered in this study. Unlike previous findings, the tip vortex ring, is derived solely
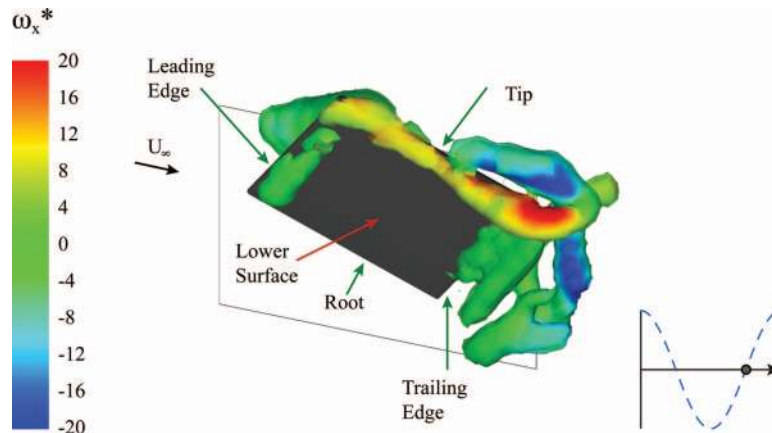

FIG. 10. An isometric view of the lower surface of the $b/c = 1$ wing at $t^* = 0.75$, for $St_c = 1.35$. Iso-surfaces represent constant Q-criterion, $Qc/U_\infty = 15$, 30, and 45 and colour maps represent streamwise vorticity.
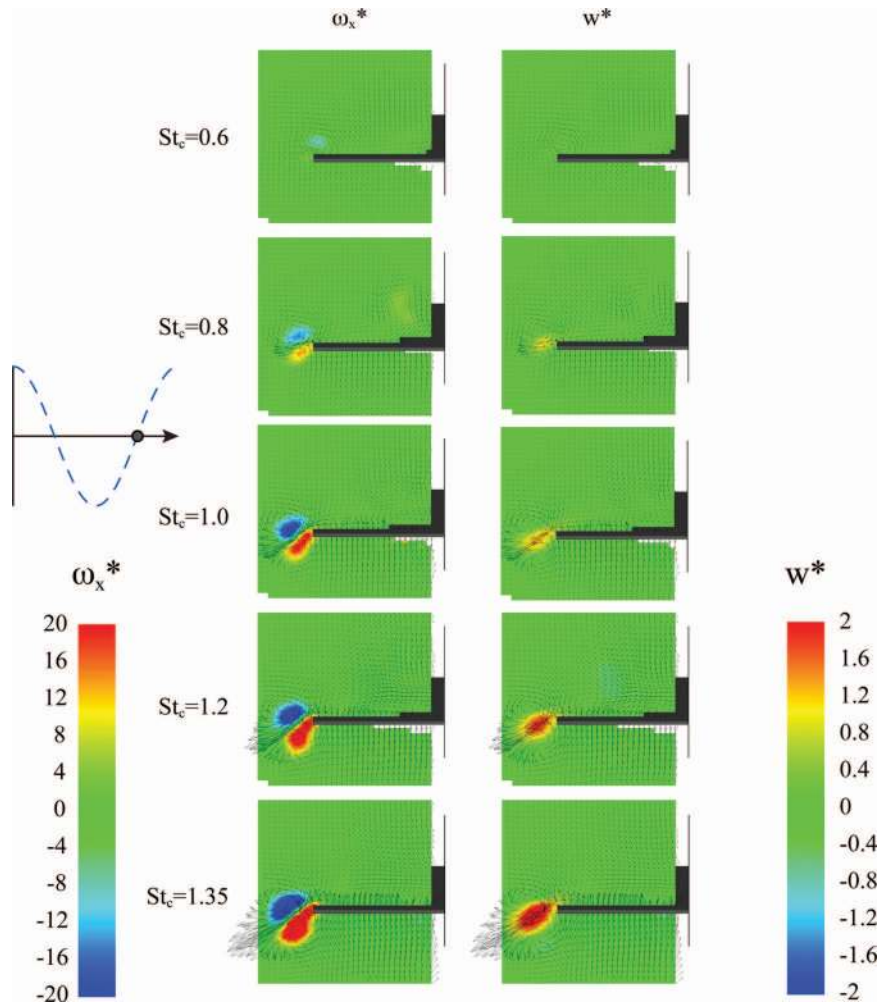
FIG. 11. Cross-stream slices through the tip vortex of the $b/c = 1$ rectangular wing, taken 0.1c from the trailing edge, show non-dimensionalised vorticity along the x-axis (left column), $\omega_x^* = |\omega_x c/U_\infty|$, and non-dimensionalised spanwise velocity (right column), $w^* = w/U_\infty$.

from the joining of two tip vortices that originate from the same wingtip, however, from different half cycles (for upward and downward motion of the wing). Uniquely, the induced velocity has a dominant spanwise component that propels the tip vortex ring in an outward direction from the tip of the wing. To the best of our knowledge, this is the first observation of such vortex rings. This phenomenon is only observed at high Strouhal numbers.

The results indicate that the tip vortex ring occurs at relatively high Strouhal numbers and it may appear that it is related to the decrease in the time-averaged lift force at high Strouhal numbers. However, there is another phenomenon that occurs at high Strouhal numbers and decreases the mean lift force: formation of lower surface leading-edge vortex. Hence, it is difficult to conclude the relative contribution of these two phenomena to the decrease in the lift force.

D. Effect of planform shape

In Figure 12, we investigate the effect of planform shape and aspect ratio, at a Strouhal number of $St_c = 0.6$. The higher aspect ratio rectangular wing engenders a very similar vortex structure to the one that appears on the lower aspect ratio rectangular wing. We observe that increasing the span
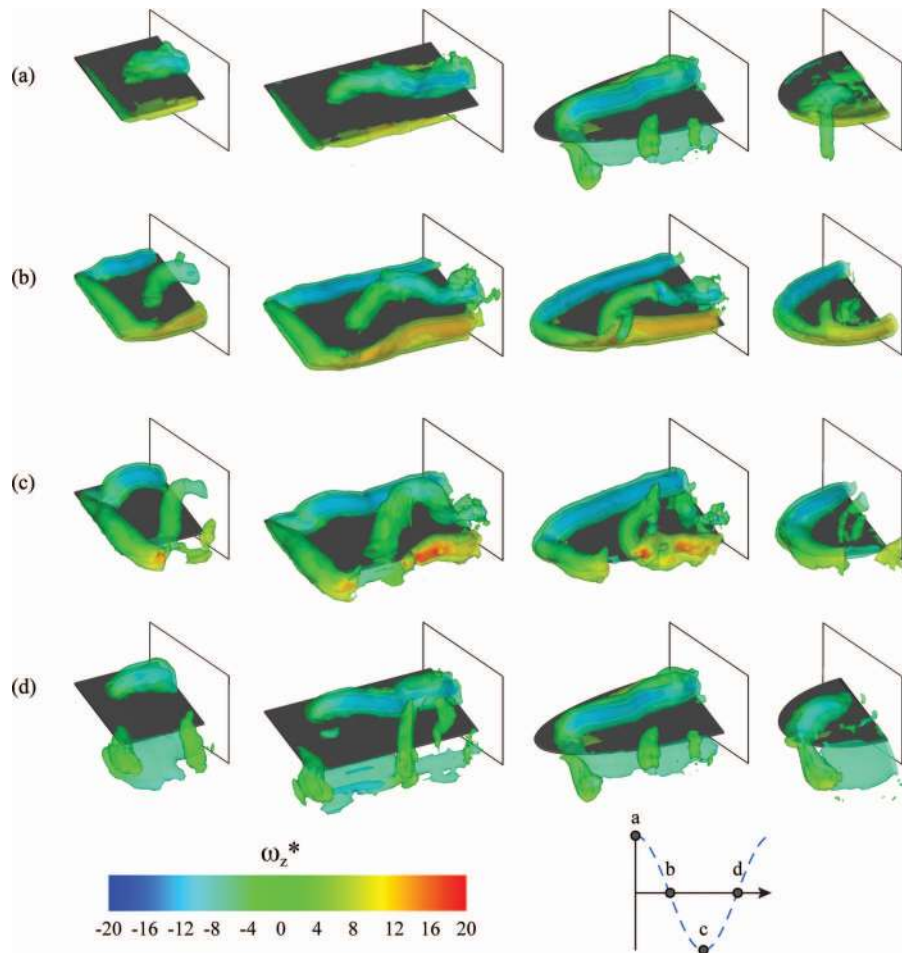
FIG. 12. (a)–(d) A comparison between planforms at $St_c = 0.6$. Iso-surfaces represent constant vorticity magnitude, $|\omega^*| = 7$, 15, and 25 and colour maps represent spanwise vorticity.

has little effect on the flow generated closer to the tip. Outboard of the wing, the LEV evolves in a very similar manner, deforming and moving inboard of the wing as it positions itself vertically on the surface of the wing. However, further inboard, the span has greater influence and the two show dissimilar flows. At the top of the oscillation, we observe that the LEV is more distorted. Moreover, as the LEV begins to deform, we fail to see half an arched shaped structure, and instead, the vortex filament is redirected back towards the surface and then levels out before it reaches the endplate. Effectively, the full span wing would encounter a double peak structure rather than a single peak structure, which then advects downstream.

Yilmaz and Rockwell[31] compared the vortical flow patterns for rectangular and elliptical wings for a pitch-up motion. In our case, we also considered the effect of an elliptical planform for periodic plunging motion. The LEV appears to deform and progress inboard in a very similar manner. While the overall filament shapes are similar, the reduction in chord length along the span of the elliptical wing has a significant impact on its interaction with the trailing edge vortex. For example, if we compare the flow at the middle of the downstroke (phase (b)), we observe how the anchor point appears to curl up, so as to match the direction of rotation of the trailing edge vortex. With respect to the tip vortex, the two planforms are quite dissimilar. The change in planform not only affects the shape and strength of the tip vortex, but it also appears to affect the "detachment" process it undergoes during the upward motion of the wing. Whereas the rectangular planform encourages a precipitant detachment from the leading edge vortex, the elliptical planform
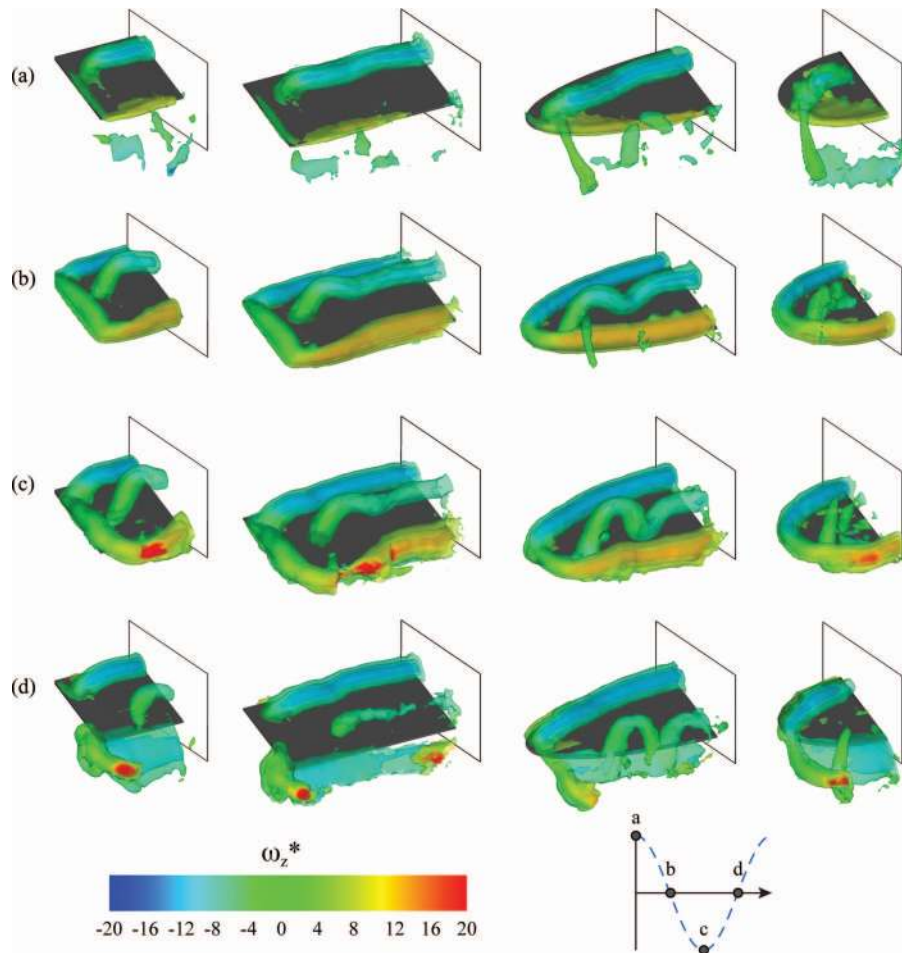
FIG. 13. (a)–(d) A comparison between planforms at $St_c = 0.8$. Iso-surfaces represent constant vorticity magnitude, $|\omega^*| = 7$, 15, and 25 and colour maps represent spanwise vorticity.

ensures a relatively slow release downstream while connected to the leading edge vortex (see phase (a)).

In Figure 13, we consider a higher Strouhal number of $St_c = 0.8$. Once again, we observe similar vortex structures at the tip of the rectangular planforms. However, in this case, the increase in Strouhal number encourages the vortex to remain more coherent in the spanwise direction, inboard of the $b/c = 2$ wing. The effect on the elliptical wing is different at this Strouhal number and instead, the leading edge vortex undergoes a remarkable transformation, developing a distinct undulation (see phase (c)). To the authors' knowledge, this is the first time that this has been reported. This Strouhal number coincides with the second peak in lift in Figure 4. During the formation of strong undulations and evolution to arch-type vortical structures, extra suction is generated on the wing surface as these structures become closer to the surface, as shown by Visbal.[11] It is interesting to see that the structure does bare some resemblance to the LEV on the rectangular wing at the lower frequency (see phase (c) in Figure 12). The overall outboard shape of the leading edge vortex is very similar. Since we have only considered a selected number of Strouhal numbers, it is possible that the extreme undulation encountered on the elliptical wing, also occurs on the rectangular wing at some intermediate Strouhal number not considered in this study. Therefore, we cannot conclude that this is simply an elliptical wing phenomenon. In fact, it will be shown later on that undulation exists for a specific Strouhal number ($St = 0.75$).
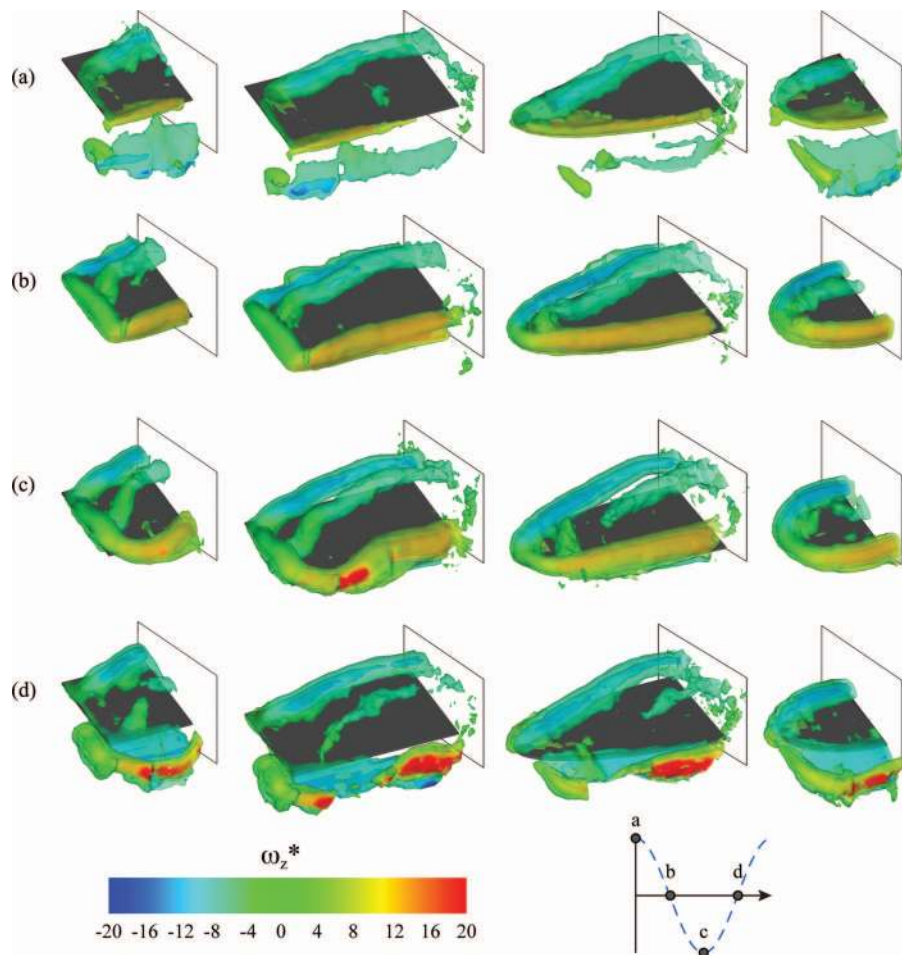
FIG. 14. (a)–(d) A comparison between planforms at $St_c = 1.0$. Iso-surfaces represent constant vorticity magnitude, $|\omega^*| = 7$, 15, and 25 and colour maps represent spanwise vorticity.

The tip vortex ring is also of particular interest. The comparison of planforms for an operating frequency of $St_c = 0.8$, indicates that the phenomenon continues to exist on the larger aspect ratio rectangular wing. Furthermore, the overall shape and positioning of the ring, appears to be unaffected by the change in span length. The effect of an elliptical planform, is considerably different in that it evidently prevents the formation of the tip vortex ring. It appears that the lower surface tip vortex is too weak for it to encourage its formation.

A similar comparison of flow structures is shown in Figure 14 at a Strouhal number of $St_c = 1.0$. The higher plunging frequency appears to dampen any strong undulations across the span of the wings. We observe instead that the LEV anchor point remains quite close to the tip, develops a strong kink, similar to that observed for the lower aspect ratio case, and moves further away from the surface further inboard of the wing. This is the case for both rectangular and elliptical planform. The considerable vertical movement, agrees well with the time-averaged measurements, which indicate a reduction in lift performance at the higher Strouhal numbers. This appears to be exacerbated by the larger span wings.

Evidently, the three-dimensional structures that reside on the surface of these plunging wings are quite complex, and require that all three velocity components be resolved to understand how these vortex filaments evolve across the surface. It is interesting to consider in more detail how the spanwise undulations form during the plunging motion. In Figure 15, we present the vortex core locations, using the Q-criterion as a core identification tool. This has been carried out for the
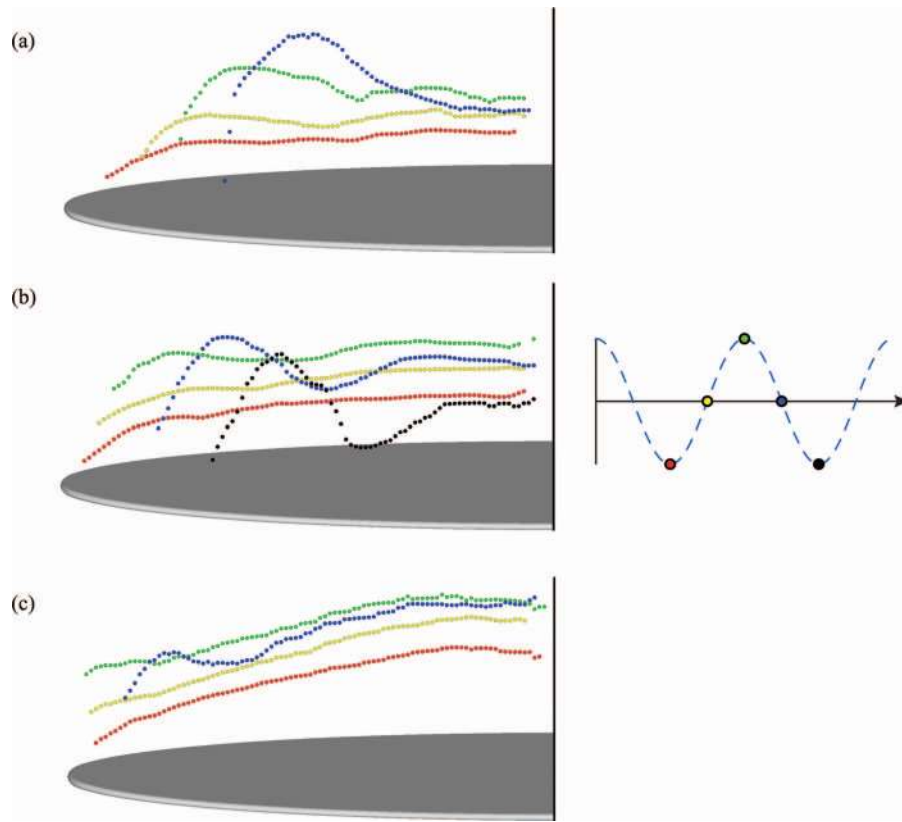
FIG. 15. Vortex core tracking for the $b/c = 2$ elliptical wing at (a) $St_c = 0.6$, (b) $St_c = 0.8$, and (c) $St_c = 1.0$, viewed from downstream of the wing. The wing corresponds to its location at the bottom of the cycle.

elliptical wing at various phases and Strouhal numbers. It allows us to more adequately superimpose the entire vortex trajectory onto a single figure. For example, we observe quite clearly the relative motion of the LEV anchor point throughout the cycle for the different Strouhal numbers, as well as how the spanwise peak in the filament travels inboard of the wing. The large undulation that we observed in Figure 13, appears in Figure 15(b). Apparently, the undulation exists quite early on in the cycle, initially existing close to the tip of the wing (see Figure 15(b) at the bottom of the cycle). As the cycle progresses, the undulation both amplifies and travels inboard. This occurs for all three Strouhal numbers, however, the change in Strouhal number alters the time scale and therefore, the progression of this "travelling wave." For example, for $St_c = 0.6$, the trough is quite close to the root of the wing, for $St_c = 0.8$, the trough is closer to the midspan of the wing, and for $St_c = 1.0$, the trough is closer to the tip of the wing, despite undergoing an entire plunging cycle.

A more intricate analysis of the progression of the undulation is shown in Figure 16 for both the elliptical and rectangular wing. This was carried out at $St_c = 0.75$ as it coincided with the second peak in the time-averaged lift (see Figure 4). Twelve phases in the cycle were used to develop this figure. We can now observe the progression of the undulation at each of the 12 phases. It is interesting to observe that the undulation appears far more prominent for the rectangular wing. This emphasises that although the phenomenon appears at a range of Strouhal numbers, its overall shape is highly sensitive to Strouhal number and is not limited to the elliptical planform. We are not able to comment whether LEV undulation may exist for other angles of attack. However, as the formation of arch-type vortical structure was observed for various wings at different angles of attack, we believe that they are general.
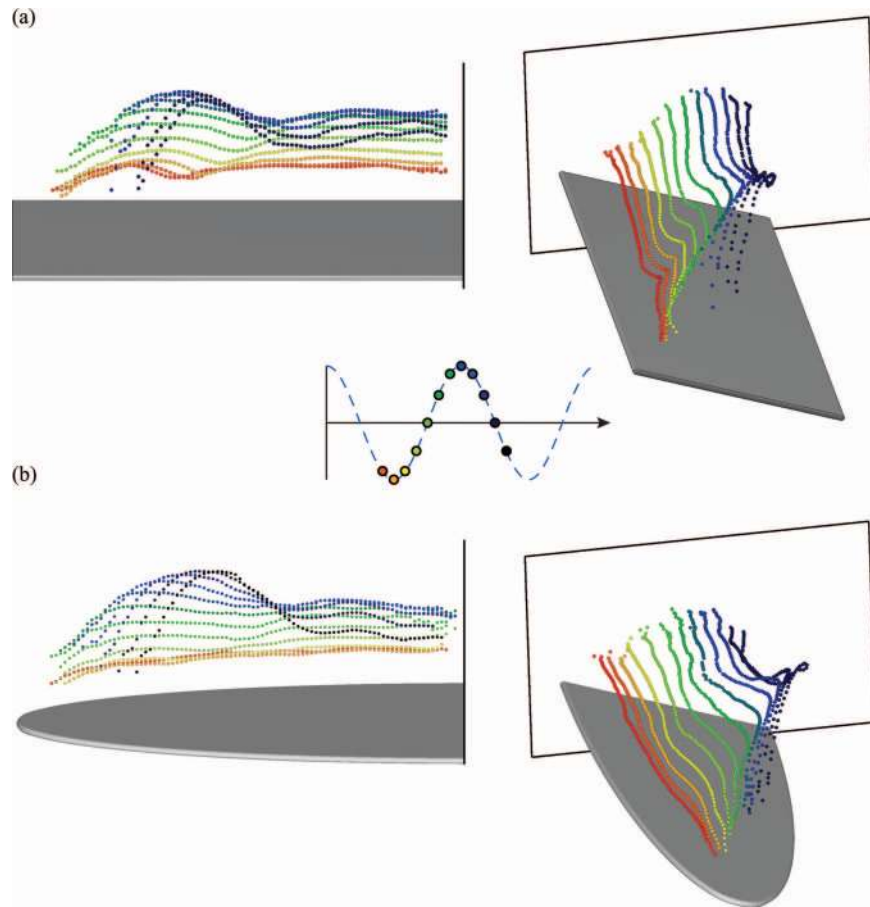
FIG. 16. Vortex core tracking for the $b/c = 2$ (a) rectangular and (b) elliptical wings, at $St_c = 0.75$, viewed from different angles. The wing corresponds to its location at the bottom of the cycle.

IV. CONCLUSIONS

A volumetric velocimetry technique has been used to analyse the three-dimensional flow generated by plunging elliptical and rectangular wings. The wings were set to a fixed geometric angle of attack of $20°$ and forced to undergo a sinusoidal vertical displacement. This study focussed on the small-amplitude oscillations. Three-dimensional vortex structures have been analysed including the formation and evolution of the leading edge vortex with respect to Strouhal number. A comparison between experimental and computed results shows good agreement between the main flow features. At low Strouhal numbers, the vortex anchors itself to the surface of the wing gradually moving inboard as the cycle progresses. Increasing the Strouhal number forces this vortex to remain closer to the tip of the wing. Several distinct fluid dynamic features have been identified including the presence of a tip vortex ring at sufficiently high Strouhal number. Vorticity iso-surface plots reveal it consists of tip vortices generated on both the downstroke and upstroke of the oscillation, despite the large positive geometric angle of attack. The tip vortex ring contains a region of strong spanwise induced velocity, propelling itself outward from the wing tip. This phenomenon is absent on the elliptical wing within a range of $St_c = 0$–1.35.

At particular Strouhal numbers, the LEV deforms significantly as it travels across the wing, in some instances developing large undulations in the spanwise direction. A vortex core identification tool has been used to illustrate its resemblance to a travelling wave that propagates inboard as the wing oscillation takes place. This phenomenon appears to be affected strongly by Strouhal number. In some cases for higher aspect ratio wings, two arched shaped vortical structures may exist on the full wing.

A lower surface leading edge vortex has also been identified, which strengthens with increasing Strouhal number. This is shown to coincide with the reduction of time-averaged lift beyond a Strouhal number range of $St_c = 0.65$–0.75. The reduction in lift is further exacerbated by the leading edge vortex moving vertically away from the wing at the higher Strouhal numbers.

ACKNOWLEDGMENTS

[1] W. Shyy, M. Berg, and D. Ljungqvist, "Flapping and flexible wings for biological and micro air vehicles," Prog. Aerosp. Sci. **35**(5), 455–505 (1999).

[2] D. J. Cleaver, Z. Wang, I. Gursul, and M. R. Visbal, "Lift enhancement by means of small-amplitude airfoil oscillations at low Reynolds numbers," AIAA J. **49**(9), 2018–2033 (2011).

[3] M. F. Platzer, K. D. Jones, J. Young, and J. C. S. Lai, "Flapping-wing aerodynamics: Progress and challenges," AIAA J. **46**(9), 2136–2149 (2008).

[4] P. Freymuth, "Propulsive vortical signature of plunging and pitching airfoils," AIAA J. **26**(7), 881–883 (1988).

[5] G. C. Lewin and H. Haj-Hariri, "Modelling thrust generation of a two-dimensional heaving airfoil in a viscous flow," J. Fluid Mech. **492**, 339–362 (2003).

[6] K. Taira and T. Colonius, "Three-dimensional flow around low-aspect-ratio flat-plate wings at low Reynolds numbers," J. Fluid Mech. **623**, 187–207 (2009).

[7] K. D. von Ellenrieder, K. Parker, and J. Soria, "Flow structures behind a heaving and pitching finite-span wing," J. Fluid Mech. **490**, 129–138 (2003).

[8] P. Blondeaux, F. Fornarelli, L. Guglielmini, M. S. Triantafyllou, and R. Verzicco, "Numerical experiments on flapping foils mimicking fish-like locomotion," Phys. Fluids **17**(11), 113601 (2005).

[9] H. Dong, R. Mittal, and F. M. Najjar, "Wake topology and hydrodynamic performance of low-aspect-ratio flapping foils," J. Fluid Mech. **566**, 309–343 (2006).

[10] T. O. Yilmaz and D. Rockwell, "Three-dimensional flow structure on a maneuvering wing," Exp. Fluids **48**(3), 539–544 (2010).

[11] M. R. Visbal, "Three-dimensional flow structure on a heaving low-aspect-ratio wing," AIAA Paper 2011-219, 2011.

[12] D. E. Calderon, Z. Wang, and I. Gursul, "Three-dimensional measurements of vortex breakdown," Exp. Fluids **53**, 293–299 (2012).

[13] F. Pereira, M. Gharib, D. Dabiri, and D. Modarress, "Defocusing digital particle image velocimetry: A 3-component 3-dimensional DPIV measurement technique. Application to bubbly flows," Exp. Fluids **29**, S078–S084 (2000).

[14] F. Pereira and M. Gharib, "Defocusing digital particle image velocimetry and the three-dimensional characterization of two-phase flows," Meas. Sci. Technol. **13**, 683–694 (2002).

[15] S. J. Baek and S. J. Lee, "A new two-frame particle tracking algorithm using match probability," Exp. Fluids **22**(1), 23–32 (1996).

[16] F. Pereira, H. Stuer, E. C. Graff, and M. Gharib, "Two-frame 3D particle tracking," Meas. Sci. Technol. **17**(7), 1680–1692 (2006).

[17] J. C. R. Hunt, A. A. Wray, and P. Moin, "Eddies, stream, and convergence zones in turbulent flows," Center for Turbulence Research Report No. CTR-S88 (Center for Turbulence Research, Stanford, USA, 1988), pp. 193–208.

[18] J. Jeong and F. Hussain, "On the identification of a vortex," J. Fluid Mech. **285**, 69–94 (1995).

[19] D. A. Anderson, J. C. Tannehill, and R. H. Pletcher, *Computational Fluid Mechanics and Heat Transfer* (McGraw-Hill Book Company, 1984).

[20] M. Visbal and D. P. Rizzetta, "Large-eddy simulation on curvilinear grids using compact differencing and filtering schemes," J. Fluids Eng. **124**(4), 836–847 (2002).

[21] M. R. Visbal, P. E. Morgan, and D. P. Rizzetta, "An implicit LES approach based on high-order compact differencing and filtering schemes," AIAA Paper 2003-4098, 2003.

[22] M. R. Visbal and D. V. Gaitonde, "High-order-accurate methods for complex unsteady subsonic flows," AIAA J. **37**(10), 1231–1239 (1999).

[23] M. R. Visbal and D. V. Gaitonde, "On the use of high-order finite-difference schemes on curvilinear and deforming meshes," J. Comput. Phys. **181**(1), 155–185 (2002).

[24] D. E. Calderon, Z. Wang, and I. Gursul, "Effect of wing geometry on the lift of a plunging finite wing," AIAA Paper 2010-4459, 2010.

[25] D. Calderon, Z. Wang, and I. Gursul, "Lift enhancement of a rectangular wing undergoing a small amplitude plunging motion," AIAA Paper 2010-386, 2010.

[26] K. Taira, C. W. Rowley, T. Colonius, and D. R. Williams, "Lift enhancement for low-aspect-ratio wings with periodic excitation," AIAA J. **48**, 1785–1790 (2010).

[27] D. J. Garmann, M. R. Visbal, and P. D. Orkwis, "Three-dimensional flow structure and aerodynamic loading on a revolving wing," Phys. Fluids **25**, 034101 (2013).

[28] M. R. Visbal, and D. Garmann, "Flow structure above stationary and oscillating low-aspect-ratio wing," in *Proceedings of the ASME 2012 Fluids Engineering Division Summer Meeting*, *FEDSM2012, Puerto Rico, USA, 8–12 July, 2012* (ASME, 2012).

[29] J. H. J. Buchholz and A. J. Smits, "On the evolution of the wake structure produced by a low-aspect-ratio pitching panel," J. Fluid Mech. **546**, 433–443 (2006).

[30] D. Kim and M. Gharib, "Experimental study of three-dimensional vortex structures in translating and rotating plates," Exp. Fluids **49**, 329–339 (2010).

[31] T. O. Yilmaz and D. Rockwell, "Flow structure on finite-span wings due to pitch-up motion," J. Fluid Mech. **691**, 518–545 (2012).